

# Statistical analysis of spatio-temporal variations of sea surface height observed by Topex altimeter

A. Fabrikant, R.E. Glazman, and A. Greysukh

Jet Propulsion Laboratory, California Institute of Technology, Pasadena CA 91109

Tel.: 818-354-7151, E-mail: reg@pacific.jpl.nasa.gov

Using non-gridded Topex altimeter data, high resolution 2-d power spectra and spatio-temporal autocorrelation functions of sea surface height (SSH) variations are estimated and employed for studying anisotropic SSH fields varying in a broad range of scales. Due to high accuracy (a few millimeters in terms of SSH variation) of the presently developed statistical technique, we find, in particular, that wavenumber spectra of SSH variation along the equator exhibit a power-law behavior  $F(k) \propto k^{-2}$  on scales from about 1000 km and up to  $10^4$  km. Based on analysis of the spatio-temporal autocorrelation, these oscillations are identified as a broad-band system of baroclinic Rossby waves whose characteristic velocity is about 1.3 m/s and the velocity of longest-wave components about 2.1 m/s. Analysis of SSH variations in the North Atlantic reveals anisotropic 2-d spectra characterized by a rapid, nearly power-law-type roll-off at wavenumbers above 0.02 rad/km. The rate of this spectral fall-off is consistent with the kinetic energy spectra of 2-d vortex turbulence. This behavior disagrees with the earlier estimates of SSH spectra.

Submitted to the Journal Of Geophysical Research, Oceans. June 1994.

## 1. Introduction

For studies of large-scale oceanic processes - particularly, equatorial waves - altimetry has no alternatives, for the broad range of **spatio-temporal** scales of oceanic motions and a high accuracy required of a measuring technique are not achievable with conventional observation systems. However, the irregular sampling and other difficulties of satellite altimeter observations necessitate development of special techniques for data analysis.

The relatively large separation of **Topex/Poseidon** (T/P) ground tracks (315 km for ascending or descending tracks at the equator) and their 10-day **repeat** cycle **determine** spatial and temporal sampling rates of T/P measurements. The accuracy of SSH determination is presently believed to be about 5 cm - in terms of the overall rms SSH error. Although this is sufficient for many problems of ocean circulation, some studies require higher accuracy and finer **spatio-temporal** resolution. An example is given by Kelvin, Rossby and other ocean waves characterized by a small amplitude and a broad range of scales.

While the magnitude of SSH variations caused by strong episodically occurring events (pulses) of equatorial waves may attain a few decimeters, the magnitude of **SSH** oscillations representing the persistent background of long waves is only about 5 cm. These oscillations are studied in section 4. Another important feature of the SSH field is its intrinsic statistical anisotropy. In section 3 we estimate two-dimensional wavenumber spectra of SSH variations at mid latitudes in the North Atlantic.

A technique suggested in the present work yields quantitative statistical characterization of SSH variability and expands the range of applications of satellite altimeter data for ocean studies. One such application might be the use of observed SSH spectra for validation of numerical models of global ocean circulation.

The approach described in Section 2 allows one to identify SSH variations with magnitude well under 1 cm, on time scales from a few days and up, and spatial scales starting at about 70 km. The analysis is presently confined to only the most basic properties

of the SSH field: its spatial autocorrelation, mixed spatio-temporal autocorrelation and wavenumber (power) spectra. However, these statistical characteristics contain a wealth of geographic as well as dynamic information - yet to be utilized in ocean studies. The 2-d spectra allow one to assess anisotropy and multiple-scale variability of the SSH field (associated with elements of geostrophic turbulence), help identify sources and sinks of kinetic energy and vorticity of two-dimensional flows, investigate (baroclinic) inertia-gravity and planetary waves (such as equatorial Rossby waves), etc. Mixed autocorrelation functions characterize wave dispersion and yield estimates of the wave propagation velocity.

While 1-d spectra (corresponding to SSH variations along satellite ground tracks) - whose estimation from altimeter data is straightforward - were extensively studied in the past years (e.g., [Fu, 1983; Le Traon et al., 1990; Mey and Menard, 1989; Le Traon, 1992]), 2-d spectra remained out of reach owing to formidable difficulties of their determination. One such difficulty is due to the fact that altimeter ground tracks do not provide a sufficiently fine and regular coverage required by standard (FFT-based) techniques of spectral analysis. Placing the data onto a regular geographic grid yields the mesh size of about two degrees. As a result, the highest wavenumbers resolved based on the gridded data are about 0.01 rad/km, and the estimation of 2-d spectra loses much of its worth. Indeed, the range of spatial scales for interesting dynamical features, - for instance, warm and cold core rings, meso-scale eddies, meanders of ocean currents, etc., - starts at tens kilometers.

The technique described in the following section permits using a small (down to two) number of satellite passes occurring in an area of interest within a short time interval (down to one day) called “the interval of synchronicity.” This approach results in a dramatic increase of the spatio-temporal resolution of the spectral analysis and, - due to averaging over a large ensemble, - it suppresses error noise in altimeter measurements. While our present discussion is focused on details of the statistical approach, section 3 and 4 provide some new data on and insight into large-scale ocean dynamics.

## 2. Evaluation of spatio-temporal autocorrelation functions and wavenumber spectra

The SSH data employed have been corrected for the sea state bias, static atmospheric pressure and various other intervening factors - as described in (Benada, 1993). The geoid and tidal (solid Earth and ocean) variations have also been removed from the data. The residual error of SSH measurements is presently believed to be about 5 cm. One particular component of this error is of special concern. This component arises from the remaining uncertainty in the satellite orbit and could introduce a slight difference in the SSH values on different satellite passes. In order to reduce possible effects of the orbit-dated SSH offset between any two tracks, we employed a conventional orbit correction routine [see, for example, (Tai, 1989) and (Zlotnicki et al., 1989)], whereby a quadratic polynomial fitted to track segments 3000 km long is subtracted from the SSH values. Since this correction may yield some undesirable high-pass filtering of SSH variations along satellite passes, we emphasize that, due to its large wavelength, this correction may distort only very large-scale SSH variations (with length scales approaching 3000 km) along the tracks.

Our approach exploits the idea of a "synchronicity interval,"  $\Delta t$ . This is the period within which SSH temporal variations are assumed to be negligible. The satellite passes occurring within this interval are treated as simultaneous. Long series (a season or a year worth) of altimeter data for a given ocean area are then broken down into a large number of (overlapping) subsets of quasi-simultaneous SSH observations. By design, each subset contains data from at least one ascending and one descending track. Using pairs of SSH points from all quasi-simultaneous tracks, we obtain SSH products  $\zeta(\mathbf{x}, t)\zeta(\mathbf{x}+\mathbf{r}, t+\delta t)$  for bins on the  $\mathbf{r}$ -plane, where  $0 < \delta t \leq \Delta t$ . The left-hand-side inequality means that the pairs of points belonging to the same altimeter pass are excluded. If the synchronicity interval is very short - as illustrated in Fig. 1 - the points generated on the  $\mathbf{r}$ -plane by any given "synchronous" subset yield only a limited coverage. Of course, as additional synchronous subsets are subsequently used, the coverage increases tending to fill the  $\mathbf{r}$ -plane. However,

a one-day **synchronicity** interval generates a highly uneven coverage (in terms of the number of point pairs available for statistical averaging within each  $r$ -bin). The most complete and uniform coverage of the  $r$ -plane is achieved by taking  $A_t$  to be the period of the orbit repeat cycle (10 days for the T/P mission). However, this would limit our consideration to relatively slow processes. In section 4, we use short synchronicity intervals to investigate relatively fast **SSH** oscillations caused by equatorial waves. A particular choice of the synchronicity interval, - hence the density and **uniformity** of the  $r$ -plane coverage, - depends on the problem at hand and on the satellite orbit configuration.

The SSH products are calculated for all synchronous subsets. Ultimately, the time difference  $\delta t$  in the products  $\zeta(\mathbf{x}, t)\zeta(\mathbf{x}+\mathbf{r}, t+\delta t)$  is ignored. Moreover, since the **SSH** field is treated as statistically stationary and spatially-homogeneous, the absolute times  $t$  and positions  $\mathbf{x}$  are also ignored. The **autocorrelation** function  $W(r)$  is ultimately found by averaging all products  $\zeta(\mathbf{x})\zeta(\mathbf{x}+\mathbf{r})$  falling into pm-set  $\Delta\mathbf{r}$ -bins (say, 20 by 20 km) on the  $\mathbf{r}$ -plane. Respectively, the bins' size determines the number,  $N(r)$ , of individual **SSH** products available for an estimation of the **autocorrelation** function at a given "point" on the  $r$ -plane,

While the above procedure usually generates an enormous number of SSH products for intermediate spatial lags, it yields few products for lags comparable to the linear size of the observed area. Therefore, in order to ensure adequate sampling for large lags, we additional] y use track segments outside the area of primary interest. These segments form, what we call, the "fringe" and are shown in Panel A of Figs. 1 and 2 by thin dotted lines. The fringe points are paired only with the inside points - to ensure pertinence of the **autocorrelation** function to the given ocean area.

The statistical error,  $\Delta W(\mathbf{r})$ , is related to the SSH measuring error,  $e$ , by  $\Delta W \approx e^2 \sqrt{N}$  where  $N(r)$  is the number of independent products  $\zeta(\mathbf{x}, t)\zeta(\mathbf{x}+\mathbf{r}, t+\delta t)$  employed to estimate  $W(r)$ . At short **synchronicity** intervals, this number is distributed in the  $r$ -plane very unevenly.

Estimation of the autocorrelation function from observation points forming a complex spatial pattern is done rather efficiently by taking pairs of points in any order and then referencing the products to a regular grid of spatial (temporal) lags. In the present work we employed 35 cycles covering 350 days of the Topex mission. In order to reduce the computer time, we sampled only every second, or even fourth, (1-sec average) SSH measurement along satellite tracks. For a case in which every 2nd SSH measurement is used, the resultant distribution  $N(\mathbf{r})$  is presented in Fig. 3 where we employed  $\Delta t = 10$  days. For a  $\Delta r$ -bin size of 20 km, the mean number of independent SSH products at a point on the  $r$ -plane is  $\langle N \rangle \approx 8.103$ . In terms of the error of  $W(\mathbf{r})$  estimation, this is  $0.28 \text{ cm}^2$  - which is equivalent to the SSH measuring accuracy of 5 mm. The minimum and maximum values of  $N(\mathbf{r})$  in a given example were 880 and  $6 \cdot 10^4$ , respectively. In order to reduce adverse effects of  $N(\mathbf{r})$  variations, the autocorrelation function is eventually smoothed to suppress its undulations on scales near the  $\Delta r$ -binsize. In the examples illustrated below,  $W(\mathbf{r})$  was smoothed using 3-point linear smoother.

Very short synchronicity intervals (1 to 4 days) result in a rather irregular coverage of the  $r$ -plane. Therefore, some kind of gridding may "sometimes become necessary in order to fill a few occasional gaps on a regular (either rectangular or polar) grid of  $W(\mathbf{r})$  values. In such (rather rare) cases, we used the Delaunay triangulation (Akima, 1978) whereby a plane is drawn through every three neighboring points  $W(\mathbf{r}_i)$ ,  $W(\mathbf{r}_j)$ ,  $W(\mathbf{r}_k)$  to produce values of the autocorrelation function at arbitrary points inside a triangle  $\mathbf{r}_i, \mathbf{r}_j, \mathbf{r}_k$ .

When calculating the wavenumber spectrum  $F(\mathbf{k})$  from  $W(\mathbf{r})$ , we employed a tapering technique (equivalent to the Hanning window used in the standard spectral analysis) which reduces the remaining effect of a finite size of the ocean area.

Before applying the technique to satellite data, it was tested on simulated random fields with known spectra. "Sea surface height" fields were generated as 2-d Gaussian random fields with a given spectrum, and a delta-correlated random noise was added to simulate measuring errors. Under conditions similar to satellite altimeter observations, the technique

showed very good performance in terms of reproducing the original autocorrelation functions and spectra.,

While the presently limited accuracy and volume of Topex observations make it difficult to accurately estimate a full 3-dimensional spectrum, it is still possible to quantify the temporal-spatial evolution of the SSH field by employing pairs of points separated by both spatial and temporal lags. Thus, we evaluate a mixed, spatio-temporal autocorrelation  $W(\mathbf{r}, \tau)$  -in section 4. The estimation of  $W(\mathbf{r}, \tau)$  is analogous to that of  $W(\mathbf{r})$ : we use SSH measurements reported at time moments “known” only to a certain accuracy (i.e., within the synchronicity interval). Therefore, the products  $\zeta(\mathbf{x}, t)\zeta(\mathbf{x}+\mathbf{r}, t+\delta t+\tau)$  will be useful for the estimation of  $W(\mathbf{r}, \tau)$  only if  $\delta t$  is sufficiently small. Specifically, the choice of the time lag is constrained by the condition:  $\delta t \ll \tau$ .

The spatio-temporal autocorrelation is of great importance for analysis of wave processes. Using a dispersion relationship,  $\omega = \omega(k)$ , the mixed autocorrelation function is related to the wavenumber spectrum by

$$\begin{aligned} W(\mathbf{r}, \tau) &= \iint \Phi(\mathbf{k}, \omega) e^{i(\mathbf{k}\mathbf{r} - \omega\tau)} d\mathbf{k} d\omega = \iint F(\mathbf{k}) \delta(\omega - \Omega(\mathbf{k})) e^{i(\mathbf{k}\mathbf{r} - \omega\tau)} d\mathbf{k} d\omega = \\ &= \int F(\mathbf{k}) e^{i\mathbf{k}[\mathbf{r} - \mathbf{c}(\mathbf{k})\tau]} d\mathbf{k} \end{aligned} \quad (1)$$

where  $\Phi(\mathbf{k}, \omega)$  is the 3-d spectrum,  $F(\mathbf{k})$  is the 2-d spectrum and  $c(k)$  is the wave phase velocity. In a non-dispersive case, (1) reduces to:

$$W(\mathbf{r}, \tau) = \int F(\mathbf{k}) e^{i\mathbf{k}(\mathbf{r} - \mathbf{c}\tau)} d\mathbf{k} = W(\mathbf{r} - \mathbf{c}\tau) \quad (2)$$

In other words, at a fixed time lag, the mixed autocorrelation function  $W(\mathbf{r}, \tau)$ , plotted as a function of  $\mathbf{r}$ , will differ from the spatial autocorrelation function  $W(\mathbf{r}, 0)$  by a uniform horizontal shift  $\mathbf{c}\tau$  about the origin. This shift is used in section 4 to estimate the characteristic velocity of Rossby waves.

in section 4, we estimate a one-dimensional spatial and two-dimensional mixed autocorrelation functions for a narrow zonal channel centered about the equator. The procedure, being similar to the evaluation of the 2-d spectra, hardly requires a detailed explanation. The only important comment here is that, at large spatial lags (for which this analysis was carried out), the Fourier transformation of  $W(r)$  can be avoided. This is because the 1-d spatial autocorrelation function, as shown in section 4, takes a very special - linear - form, This form is known to yield asymptotic wavenumber spectrum  $F(k) \propto k^{-2}$  in the high-wavenumber range (e.g., Glazman and Weichman, 1989). In general, the high-wavenumber range of a 1-d spectrum is given by

$$F(k) \propto k^{-3+2\mu}, \quad (3)$$

which, for  $\mu > 0$ , corresponds to the short-range asymptotic of the autocorrelation function

$$W(r) \approx W(0) - Cr^{2-2\mu} \quad (4)$$

where  $W(0)$  and  $C$  are constants. Hence, when  $W(r)$  exhibits a linear behavior, the spectrum rolls off as  $k^{-2}$ .

### 3. Characteristic features of the SSH field at mid-latitudes in the North Atlantic

Let us illustrate the technique by estimating 2-d power spectra  $F(\mathbf{k})$  of SSH spatial variations in the North Atlantic. In the absence of gravity waves (such as barotropic or baroclinic inertia-gravity waves), the SSH variations represent a response of the free surface to the vertical component of oceanic motion (eddies, rings, currents, etc.). These variations are relatively slow. Hence, estimating  $F(\mathbf{k})$  in a  $10 \times 10$  degree area with a synchronicity interval large enough to filter out possible gravity waves, one anticipates to find spectra compatible with the  $k^{-3}$  and/or  $k^{-5/3}$  spectral densities of kinetic energy of 2-d turbulence (for enstrophy and energy spectral cascades, respectively). Based on the geostrophic



relationship, the SSH power spectrum should fall **of** as  $k^{-5}$  (in terms of the 1-d spectrum defined by (5)), but no slower than  $k^{-1/3}$ .

Figure 4 shows regions selected to test our technique. In Figures 5 and 6, the autocorrelation function and wavenumber spectrum are presented for Region 2 in the North Atlantic for a 5-day synchronicity interval. The same functions calculated for a 10-day synchronicity interval are shown in Figs. 7 and 8. Evidently, the difference between the two cases is rather small, indicating that the main features shown in Figs 5 and 6 do not change on time scales of several days. The spectrum exhibits considerable anisotropy and distinct spectral peaks. The main peak corresponds to about 0.015 rad/km, which points to the spatial scale of about 400 km for most energetic SSH variations in this region. Figures 9 and 10 illustrate  $W(r)$  and  $F(k)$  for Region 1. In Figure 11, we present orthogonal sections of these spectra. Figures 6-11 show that, depending on the orientation of altimeter ground tracks, linear sections of the autocorrelation function and of the 2-d spectrum maybe exhibit considerable differences. Hence, 1-d spectra based on individual (ascending or descending) passes do not generally provide unambiguous spectral information.

We also find it highly interesting that in some ocean regions, our results disagree with the spectra reported by other investigators (e.g., with **Le Traon** and **Rouquet**, 1990). In the previous studies, SSH spectra were calculated using data from ascending and descending tracks separately. Assuming an approximate statistical isotropy of the SSH field, **Le Traon** et al. presented the averages of these two spectra. [To ensure that our data are statistically consistent with those used by **Le Traon** et al., we repeated their along-the-track calculations and found that the resultant 1-d spectra are in excellent agreement with the spectra reported by **Le Traon** et al.] For the purpose of the present comparison, we reduced our 2-d spectra  $F(k, \theta)$  to a 1-d form

$$F(k) = \int_{-\pi/2}^{\pi/2} F(k, \theta) k d\theta \quad (5)$$

This spectrum, plotted in Fig. 12 for Regions 1 and 2, exhibits a spectral fall-off in agreement with the 2-d vortex turbulence theory: we find  $F(k) \propto k^{-4}$  - consistent with the kinetic energy spectra mentioned earlier. In contrast to our procedure, the SSH measurements employed by the previous authors were virtually instantaneous (a 1000 km ground track segment is sampled by a satellite within 3 minutes). In terms of our synchronicity interval, this means  $\Delta t = 0$ . In a number of North Atlantic regions, particularly in the two regions used in our analysis, the 1-d spectra found by Le Traon et al. showed a rather slow spectral fall-off from  $F(k) \propto k^{-3}$  to  $F(k) \propto k^{-3/2}$ .

A possible explanation of this discrepancy can be suggested based on the following argument. Using SSH data obtained by a virtually instant sampling along the tracks, the previous authors were able to detect fast SSH oscillations related to the gravity wave mode of oceanic motions. Although the tidal components had been removed from the SSH signal, other (less well known) components were not. Inertia-gravity waves are persistent in the ocean due to a virtually permanent external and "internal" forcing. Owing to their relatively large amplitude (in terms of the thermocline depth oscillation) and small phase velocity, "baroclinic waves have a sufficient degree of nonlinearity and large enough life-time to produce a developed inertial cascade of wave turbulence. The external forcing is provided by random fluctuations of atmospheric pressure and by wind stress variations, whereas by the "internal" forcing we mean various types of hydrodynamic instability of ocean currents and jets, the radiation of gravity and/or Rossby waves by moving eddies (e.g., Stepanyants and Fabrikant, 1992), etc. Therefore, the energy source is practically permanent making spectral fluxes of the wave energy and action feasible. Recently, Falkovich and Medvedev (1992) predicted a theoretical spectrum for this situation. In terms of (5), their result is  $F(k) \propto k^{-7/3}$ . This is in reasonable agreement with some of the estimates presented by Fu (1983), De Mey and Menard (1989), Le Traon and Rouquet (1990) and other authors.

#### 4. Equatorial wave observations

Large-scale zonal motion in the Equatorial Pacific can be deduced from a sequence of SSH contour plots by tracking propagation of individual, conspicuous features of the SSH field (e.g., [Delcroix et al. 1991]). However, this (rather qualitative) approach permits positive identification of only rather large pulses of equatorial waves occurring episodically. Quantitative analysis of stationary, broad-banded SSH variations (having small amplitude and representing equatorial wave regime) calls for more elaborate, statistical techniques. As shown below, wave motions characterized by broad spectra would require a millimeter accuracy of SSH determination if conventional (deterministic) techniques of altimeter data analysis are to be employed.

The resolution of our analysis of equatorial waves is limited to spatial scales about 200 km and time scales about 10 days. We consider SSH spatial and temporal variations in a narrow zonal channel - 1.0 degree wide and 12,200 km long - across the entire equatorial Pacific. The altimeter ground tracks for a small segment of the equatorial region are illustrated in Fig 13 to show that the crossover points required for short spatial lags are located at  $\pm 2^\circ$  latitudes - beyond the narrow zonal band selected for our analysis. We subsampled SSH measurements by extracting every fourth point along the tracks. This allowed us to calculate a set of 1-d autocorrelation functions  $W(r; y=\text{const})$  for several latitudinal positions,  $y$ , within the zonal channel;  $r$  is the spatial lag along the equator. We selected the synchronicity interval  $\Delta t = 4$  days. On the one hand, this interval is sufficiently short to permit accurate estimation of the mixed autocorrelation function  $W(r, \tau)$  with  $\tau$  down to 10 days; on the other hand, this  $\Delta t$  is large enough to yield a sufficiently dense coverage of the  $r$ -axis. In Fig. 14 we illustrate effect of the synchronicity interval on the shape of the spatial autocorrelation function for the equatorial Pacific (averaged within a 1 degree zonal channel). Apparently,  $\Delta t = 2$  days is sufficient to bring out the basic (linear) behavior at large scales which is then observed in all subsequent panels of Fig. 14. However, the 2-day synchronicity interval results in a rather sparse coverage of the  $r$ -axis leaving only two points ( $r = 1200$  km and  $r = 0$  km) - to describe  $W(r)$  near the origin. Panels (c) and (d) of

Fig. 14 show that the linear regime in  $W(r)$  is confined to scales from about 1200 to 9000 km.

The mixed autocorrelation function  $W(r, \tau)$  shown in Fig. 15 represents the result of latitudinal (i.e., over  $y$ ) averaging of several  $W(r, \tau; y=\text{const})$  calculated for each latitude,  $y$ . Figures 14-15 point to the existence of two regimes of SSH spatial variations. The short-scale variations responsible for a sharp spike at the origin have spatial scales under 1000 km and are characterized by the SSH variance  $\langle \eta^2 \rangle \approx 10 \text{ cm}^2$ . These variations may be caused by rapid SSH oscillations associated with shorter equatorial waves, possibly eastward propagating Kelvin or Yanai waves. Their investigation would require an elaborate analysis going far beyond the scope of the present work. The long-range variations (corresponding to the linear range in  $W(r)$ ) have spatial scales up to 10,000 km. Their amplitude,  $\langle \eta^2 \rangle^{1/2} \approx 3 \text{ cm}$ , is found as  $\sqrt{W(\Lambda)}$  where  $\Lambda$  is the characteristics distance ( $\Lambda \approx 10^3 \text{ km}$ ) at which  $W(r)$  starts displaying the linear trend.

The most interesting and unexpected feature of the SSH field observed in Figs. 14-15 is the linear behavior of  $W(r)$  on scales from about 1000 km and up to almost the basin size scale. In accord with (3) and (4), this corresponds to the 1-d wavenumber spectrum  $F(k) \propto k^{-2}$ . The nature of SSH oscillations on these scales can be inferred from  $W(r, \tau)$  in Fig. 15. Ignoring for a moment the distortion of  $W(r, \tau)$  near the peak, we notice a gradual westward propagation of the entire shape. Therefore,  $W(r)$  of Figs. 14-15 represents a broad-banded system of westward propagating waves whose characteristic phase speed,  $\bar{c}$ , is found as

$$\bar{c} = \frac{\Delta r(\tau)}{\tau} \quad (6)$$

where  $\Delta r(\tau)$  is the westward displacement of the autocorrelation structure overtime  $\tau$ .

Based on several plots of  $W(r, \tau)$  for different values of  $\tau$  we find  $\bar{c} \approx 1.3 \text{ m/s}$  which is in agreement with the previously known estimates, e.g. (Delcroix et al., 1991). To estimate the maximum velocity,  $c_0$ , (of longest waves) one should take into account wave dispersion. The dispersion distorts the shape of  $W(r, \tau)$  as  $\tau$  increases above 10 days. Its

study is facilitated by using a simple spectral model of planetary waves - as done in the Appendix - which ultimately yields an estimate  $c_0 \approx 2.1$  m/s - in agreement with the present knowledge on equatorial baroclinic Rossby waves (e.g., LeBlond and Mysak, 1978).

The smearing of  $W(r, \tau)$  near the peak, at  $\tau > 0$ , is of great interest. Two main factors responsible for the round shape of  $W(r, \tau)$  are: (i) the vanishing of the sharp spike related to short-scale SSH variations and (ii) the weak dispersion of Rossby waves. The latter is considered in the Appendix, while the former can be explained as follows. If the short-range variations are due to some kind of equatorial waves, their absence in Fig. 15 would indicate that such waves propagate eastward and/or have a relatively short life-time. If, however, these variations are associated with slow vertical motions (mesoscale eddies) possessing no dispersion law, the vanishing of the spectral spike would confirm a non-wave-like nature of these variations.

Strong meridional variations associated with the lateral structure of the equatorial waveguide are responsible for a considerable spatial inhomogeneity of the SSH field in the direction across the equator. Therefore, our analysis is limited to a narrow zonal band - well inside the  $\pm 20^\circ$  latitudes (known as the critical latitudes [LeBlond and Mysak, 1978] for the trapped modes). Since the T/P altimeter ground tracks - Fig. 13- have no crossover points within this band, we were not able to analyze short-scale SSH variations. However, under a different orbit configuration, such analysis would be possible.

## 5. Discussion and conclusions

The statistical technique described in section 2 and illustrated in sections 3 and 4 allows one to analyze variations of 2-dimensional, time-varying fields in a broad range of spatial and temporal scales. Based on the concept of a synchronicity interval, this method has great advantages over traditional techniques of satellite data analysis which only employ data specified on a regular grid. Apparently, a similar approach can be used to estimate

higher-order statistical moments containing information about irregular, intermittent events of SSH variations. The main drawback of the present technique is the lack of a solid theoretical basis. The applications illustrated in sections 3 and 4 and the tests of the technique on simulated data (mentioned in section 2) provide empirical confirmation that the results (such as 2-d spectra and spatio-temporal autocorrelation functions) are meaningful and accurate. However, the range of conditions (i.e., the spatial and temporal separation of satellite passes, characteristic times of oceanic motions being measured, degree of statistical spatial inhomogeneity and non-stationarity of measured fields, etc.) under which the technique yields useful results remains largely unknown.

In addition to the SSH field analysis, the technique can be applied, without any major modifications, to surface wind or significant wave height observations by a satellite altimeter. Applications to other satellite measurements (SAR, scatterometer, etc.) would require modifications to account for the two-dimensional nature of these instruments' sampling within their swaths.

Two applications considered in sections 3 and 4 yielded the following conclusions:

1) SSH variations whose characteristic time scales exceed five days (in terms of the synchronicity interval  $\Delta t$ ) produce energy spectra (5) with the spectral fall-off as steep as  $k^{-4}$ . This behavior agrees with predictions of the 2-d turbulence theory. The disagreement with the earlier estimates - e.g. by Fu (1983), De May and Menard (1989), Le Traon and Rouquet (1990) and Le Traon (1992) - is explained as a result of possible manifestations of the inertia-gravity wave turbulence in the SSH spectra: the wave turbulence is observed when SSH measurements are taken within a sufficiently short time interval - as is the case when the spectra are estimated based on individual satellite passes.

2) In a wide range of scales (from about 1000 to 9,000 km), 1-d spectra of equatorial baroclinic Rossby waves exhibit a power-law behavior  $F(k) \sim k^{-2}$ . Spatio-temporal autocorrelation function (hence, its various functional, such as complex wavenumber-

frequency spectra, etc.) yield quantitative characterization of planetary waves, including estimation of their dispersive properties and characteristic speeds.

## APPENDIX: EFFECT OF WAVE DISPERSION

In a case of weakly-dispersive waves, such as equatorial trapped planetary waves,  $W(r, \tau)$  provides highly useful information. The following simple model allows one to relate parameters of equatorial waves with the observed features of the autocorrelation function.

We are concerned with the case when the internal Rossby radius of deformation,

$$R = \left( \frac{\sqrt{g'h}}{2\beta} \right)^{1/2}, \quad (A1)$$

is small compared to the characteristic length of the equatorial waves:  $Rk_0 \ll 1$ . Here,  $\beta \approx 2.3 \cdot 10^{-11} \text{ (m s)}^{-1}$  and  $\sqrt{g'h} \approx 2 \text{ m/s}$ . The phase speed of weakly dispersive waves can be written, with a sufficient degree of generality, in the form:

$$c(k) \approx c_0 (1 - \epsilon k^2) \quad (A2)$$

In the case of trapped Rossby waves,  $c_0$  and  $\epsilon$  are

$$c_0 = -\frac{\sqrt{g'h}}{2m+1}, \quad \epsilon = \frac{R^2}{m+1/2} \quad (A3)$$

with  $m$  being the number of the horizontal wave mode. To avoid imposing a particular theoretical dependence on  $c_0$  and  $\epsilon$  we shall use (1) in the non-dimensional form:

$$\tilde{W}(\tilde{r}, \tilde{\tau}) = \int_0^\infty \tilde{F}(\kappa) \exp[iQ\kappa(\tilde{r} - \tilde{\tau}) + i\tilde{\epsilon}\tilde{\tau}\kappa^3] d\kappa \quad (A4)$$

The non-dimensional variables and parameters can be expressed in terms of  $R$ ,  $c_0$  and  $k_0$  as follows:

$$\kappa = k / k_0, \quad \tilde{r} = r/L, \quad \tilde{\tau} = \frac{c_0}{L} \tau, \quad Q = k_0 L, \quad \tilde{\epsilon} = \frac{(k_0 R)^2 Q}{m + \frac{1}{2}} \quad (A5)$$

In our numerical experiment with (A4), we shall determine the value of  $\tilde{\epsilon}$  that yields the same relative reduction of  $W(r, \tau)$  near the peak as is observed in Fig. 15 at large  $\tau$ .

The desirable properties of the wavenumber spectrum are: a sharp low-wavenumber cutoff at  $\kappa \approx 1$  and a  $\kappa^{-2}$  power-law behavior at  $\kappa > 1$ . These are achieved by choosing, for instance

$$F(\kappa) = \exp(-1/\kappa^4) \kappa^{-2} \quad (\text{A6})$$

In Fig. 16, the real part of (A4) is plotted based on numerical integration with the wave dispersion parameter  $\tilde{\epsilon} = 0.1$ . This value results in about a 50 percent decrease of  $W(r, \tau)$  in the peak region for finite  $\tau$ , which is in agreement with the observations shown in Fig. 15. Greater values of  $\tilde{\epsilon}$  would yield a deeper reduction of the near-peak values of  $W(r, \tau)$ . Relationships (AS) indicate that  $\tilde{\epsilon} = 0.1$  is not unreasonable: with the spatial scale  $L \sim 10^3$  km, wavelength  $2\pi/k_0 \sim 2 \cdot 10^3$  km and internal Rossby radius  $R \sim 100$  km, (AS) yields  $Q \approx 3$  and  $\tilde{\epsilon} \sim 10^{-1}$ . In the absence of dispersion, the autocorrelation structure (a dashed line in Fig. 16) propagates about 1.6 times as fast as it does in the presence of dispersion. This allows one to estimate the value of  $c_0$  as  $1.6 * \tilde{c} \approx 2.1$  m/s.

**ACKNOWLEDGMENTS:** This work was performed at the Jet Propulsion Laboratory, California Institute of Technology, under contract with the National Aeronautics and Space Administration. The authors also thank participants of the 1994 Ocean Sciences Meeting in San Diego for useful discussions of this work.



## BIBLIOGRAPHY:

Akima, H. A method of bivariate interpolation and smooth surface fitting for irregularly distributed data points. *ACM Transactions on Mathematical Software*, 4, 143-149, 1978.

Benada, R. Merged GDR (Topex/Poseidon) Users Handbook, Version 1, Publication of the Jet Propulsion Laboratory, D-11 007, September, 1993.

De Mey, P. and Y. Menard. Synoptic analysis and dynamical adjustment of GEOS 3 and Seasat altimeter eddy fields in the Northwest Atlantic. *J. Geophys. Res.*, 94(C5), 6221-6230, 1989.

Delcroix T., Picaut J., and Eldin G. Equatorial Kelvin and Rossby waves evidenced in the Pacific ocean through Geosat sea level and surface current anomalies, *J. Geophys. Res., Oceans*. 96, 3249-3262. 1991.

Falkovich, G.E. and S.B. Medvedev. Kolmogorov-like spectrum for turbulence of inertial-gravity waves. *Europhys. Let.* 19(4), 279-284, 1992.

Fu, Lee-Lueng. On the wavenumber spectrum of oceanic mesoscale variability observed by the Seasat altimeter. *J. Geophys. Res.*, 88(C7), 4331-4341, 1983.

Glazman, R. E., and P. Weichman. Statistical geometry of a small surface patch in a developed sea. *J. Geophys. Res.*, 94(C4), 4998-5010, 1989.

Le Traon, P.Y. Contribution of satellite altimetry to the observations of oceanic mesoscale variability. *Oceanologica Acta*, 15(5), 441-457, 1992.

Le Traon, P.Y. and M.C. Rouquet, 1990. Spatial scales of mesoscale variability in the north Atlantic as deduced from Geosat data. *J. Geophys. Res.*, 95(C1 1), 20,267-20,285.

LeBlond, P.H. and L.A. Mysak. *Waves In "The Ocean*. Elsevier, New York, 1978.

Stepanyants Yu.A., Fabrikant A.L. "Features of the Cherenkov emission of drift waves in hydrodynamics and in plasma" - *Sov.Phys. JETPH*, 75(5), 818-824, 1992.

Tai, C.-K. , Accuracy assessment of widely used orbit error approximations in satellite altimetry and its oceanographic implications, *J.Atm Oceanic Techn.*, 6, 147-150, 1989.

Zlotnicki V., L.-L. Fu, and W. Patzert, Seasonal Variability in Global Sea Level observed with Geosat altimetry, *J. Geophys.Res.* 94 (C1 2), 17,959-17,970, 1989.

## Captions for Figures

Figure 1. Panel A: Altimeter ground tracks passing through Region 1 (the inner rectangle) within a 1-day period. Thin dotted lines in the outer region represent “fringe” segments of satellite groundtracks. Panel B: r-points for tracks in panel A. Here, SSH measurements are sampled every 4th point along the tracks.

Figure 2. Panel A: Altimeter ground tracks passing through Region 1 within a 4-day period, Panel B: r-points for tracks in panel A. Here, SSH measurements are sampled every 4th point along the tracks.

Figure 3. The number of SSH products  $N(\mathbf{r})$  used for calculation of  $W(\mathbf{r})$  for Region 2.

Figure 4. Ocean regions selected for analysis..

Figure 5. Spatial autocorrelation function  $W(\mathbf{r})$  (normalized by  $W(0) = 0.0021 \text{ m}^2$ ) for Region 2 based on a 5-day synchronicity interval. Thick solid contours represent level  $W(\mathbf{r})=0$ . Thin solid contours represent levels: 0.05, 0.1, 0.3, and 0.8. Dashed contours represent levels: -0.10 and -0.15.

Figure 6. Two-dimensional wavenumber spectrum,  $F(\mathbf{k})$ , corresponding to  $W(\mathbf{k})$  in Fig. 5.

Figure 7. Spatial autocorrelation function  $W(\mathbf{r})$  (normalized by  $W(0) = 0.0024 \text{ m}^2$ ) for Region 2 based on a 10-day synchronicity interval. Contours are drawn as explained in Fig. 5.

Figure 8. Two-dimensional wavenumber spectrum,  $F(\mathbf{k})$ , corresponding to  $W(\mathbf{k})$  in Fig. 7.

Figure 9. Spatial autocorrelation function  $W(\mathbf{r})$  (normalized by  $W(0) = 0.0210 \text{ m}^2$ ) for Region 1 based on a 10-day synchronicity interval. Contours are drawn as explained in Fig. 5.

Figure 10. Two-dimensional wavenumber spectrum,  $F(\mathbf{k})$ , corresponding to  $W(\mathbf{k})$  in Fig. 9.

Figure 11. 1-d sections of 2-d spectra: Spectral cross section along the zonal wavenumber is shown by the diamond-marked curve; Spectral cross section along the meridional wavenumber is shown by the crosses-marked curve. Panel A corresponds to Figs.8, Panel B corresponds to Fig, 10.

Figure 12. 1-d spectra, calculated using eq(5). Dashed line represents a power-law spectrum  $k^{-4}$ . Panel A is based on  $F(k)$  of Fig. 8, Panel B is based on  $F(k)$  of Fig. 10.

Figure 13. Satellite ground tracks in a zonal band of equatorial Pacific.

Figure 14. One-dimensional spatial autocorrelation function,  $W(r)$ , for the area  $160^{\circ}$ - $280^{\circ}$ W,  $0.5^{\circ}$ - $0.5^{\circ}$ N, for several values of the synchronicity interval: a)  $\Delta t = 1$  day, b)  $\Delta t = 2$  days, c)  $\Delta t = 7$  days, d)  $\Delta t = 10$  days.

Figure 15. Mixed autocorrelation functions,  $W(r, \tau)$ , for the equatorial Pacific region described in Fig. 13, for time lags,  $\tau$ : 10,20, 30,40, 50, and 60 days.

Figure 16. The non-dimensional mixed autocorrelation function  $W(r, \tau)$  based on (A4) with  $Q=3$ . Numbers at the curves give values of  $\tau$ . Solid curves:  $\tau > 0$  and  $\epsilon = 0.1$ . The dashed curve with  $\tau = 0.7$  is based on  $\epsilon = 0$ .

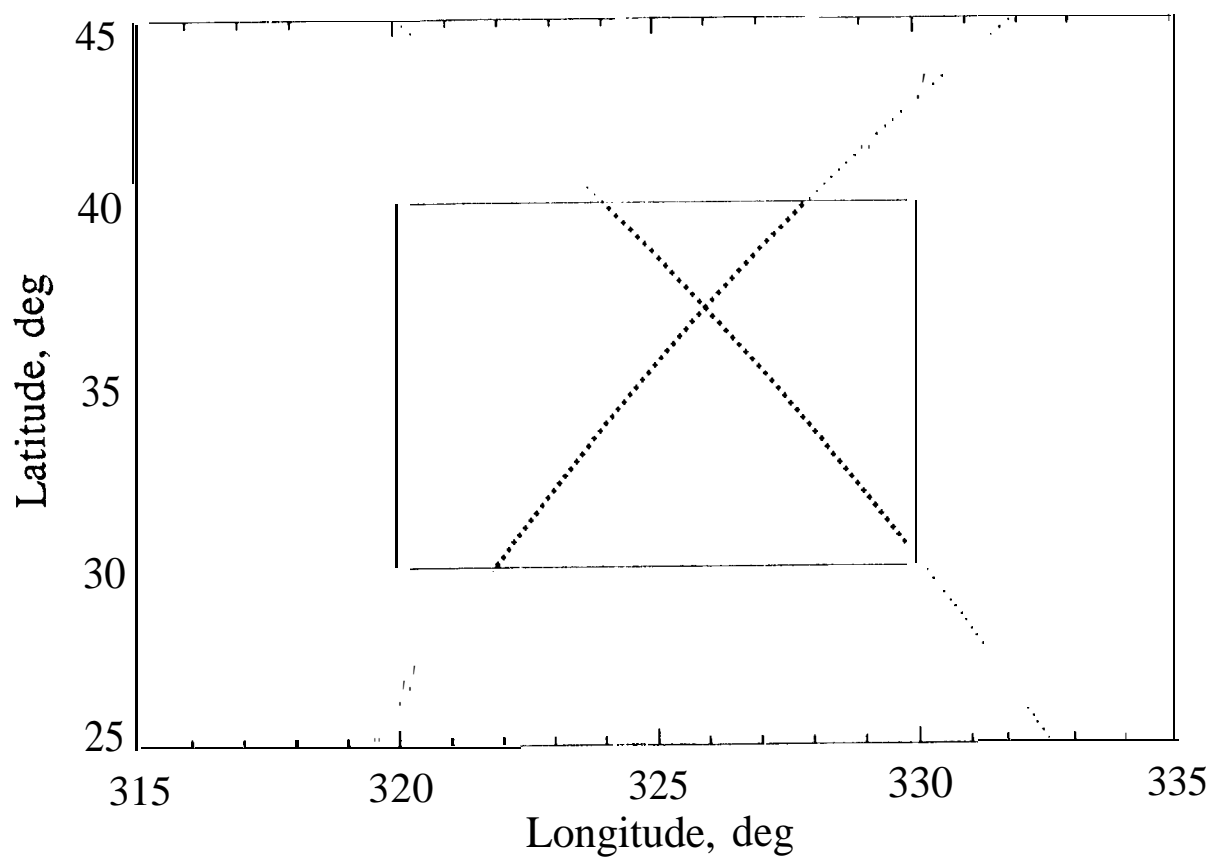


Fig. 1. Panel A.

Panel A

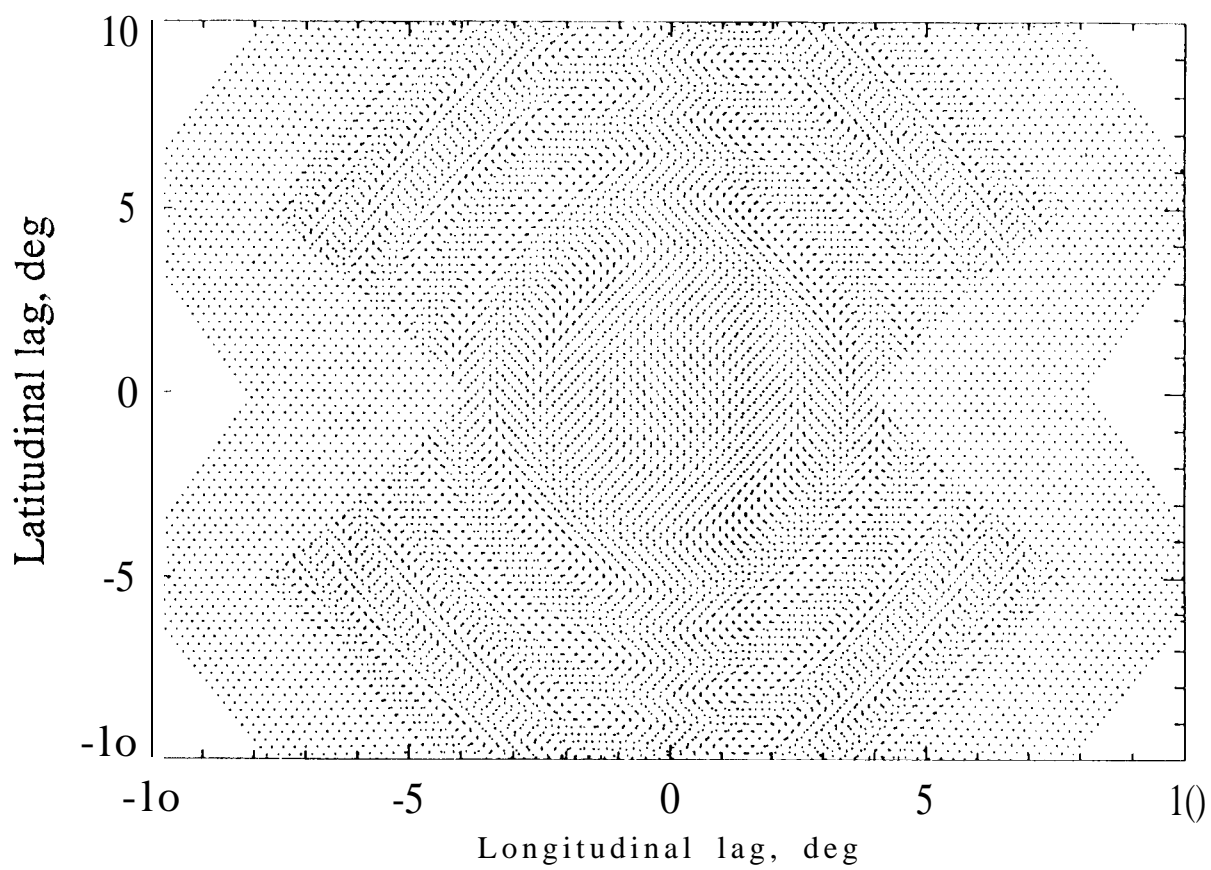


Fig. 1. Panel B

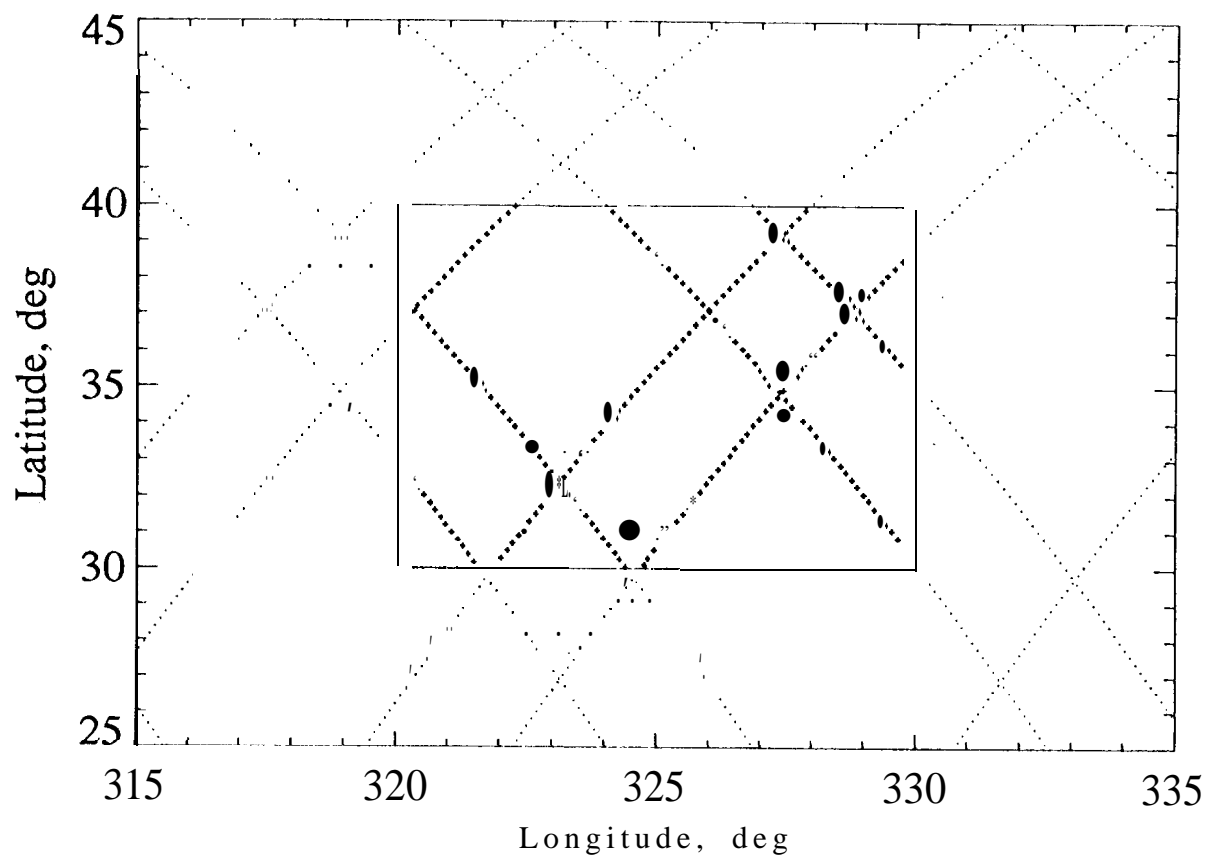


Fig. 2. Panel A.

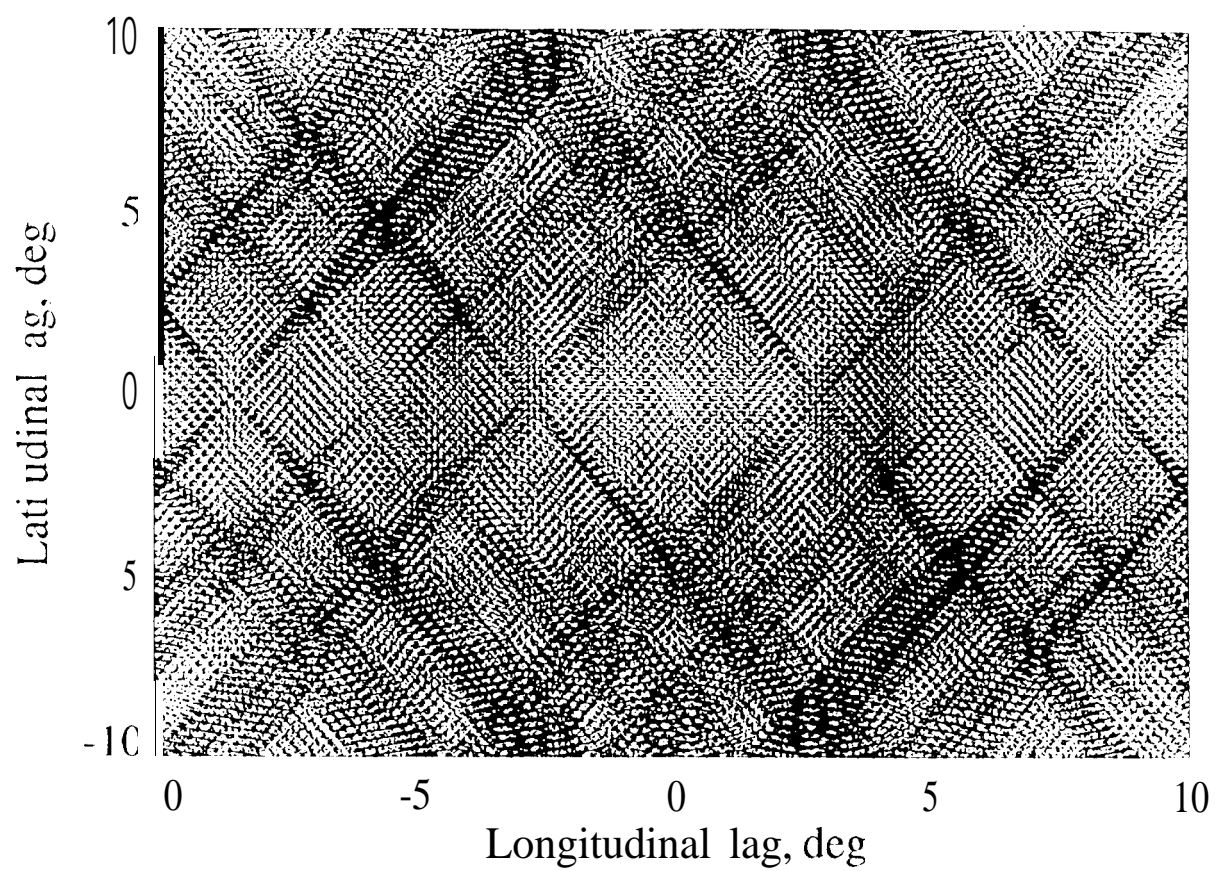
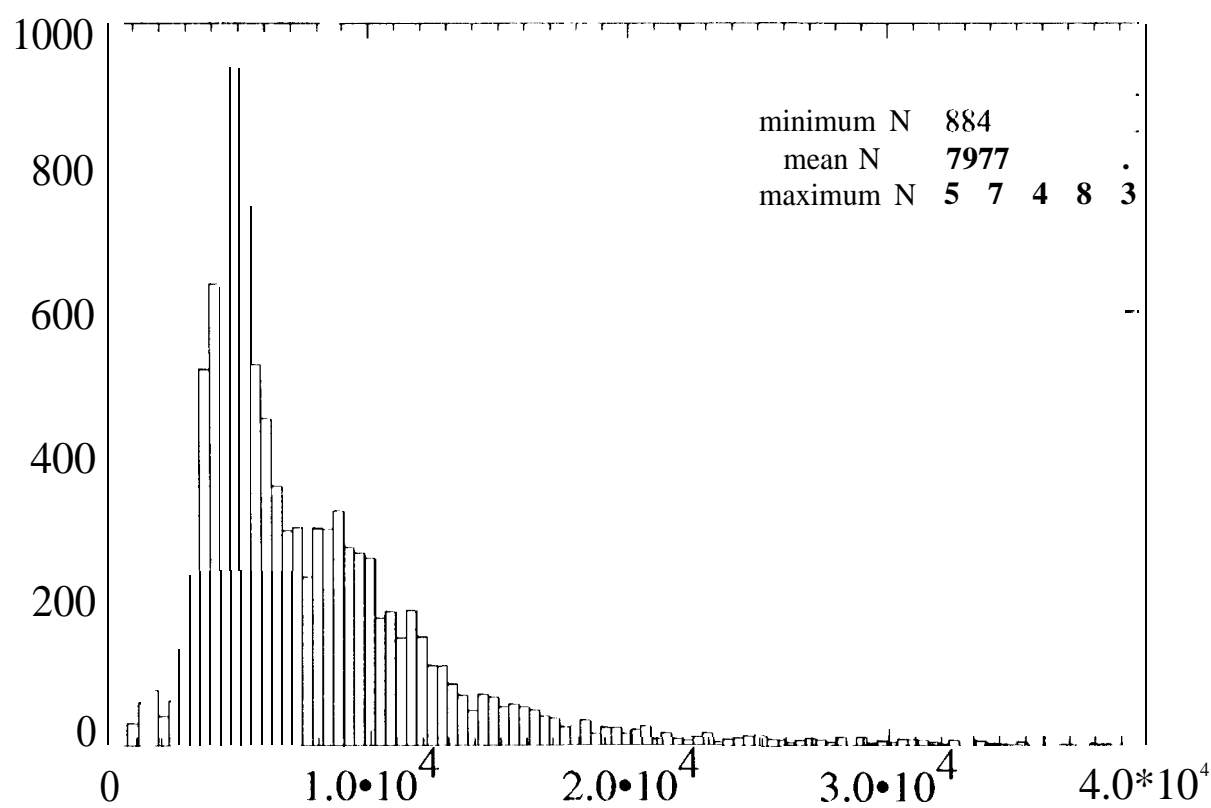


Fig. 2, B





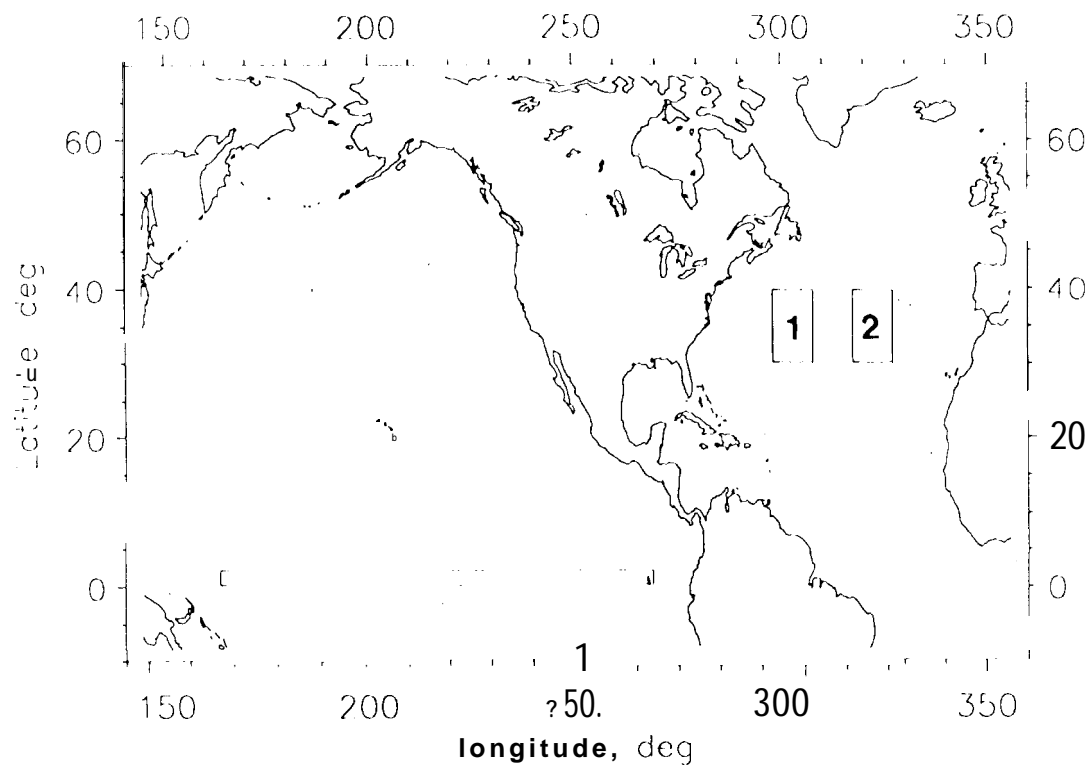
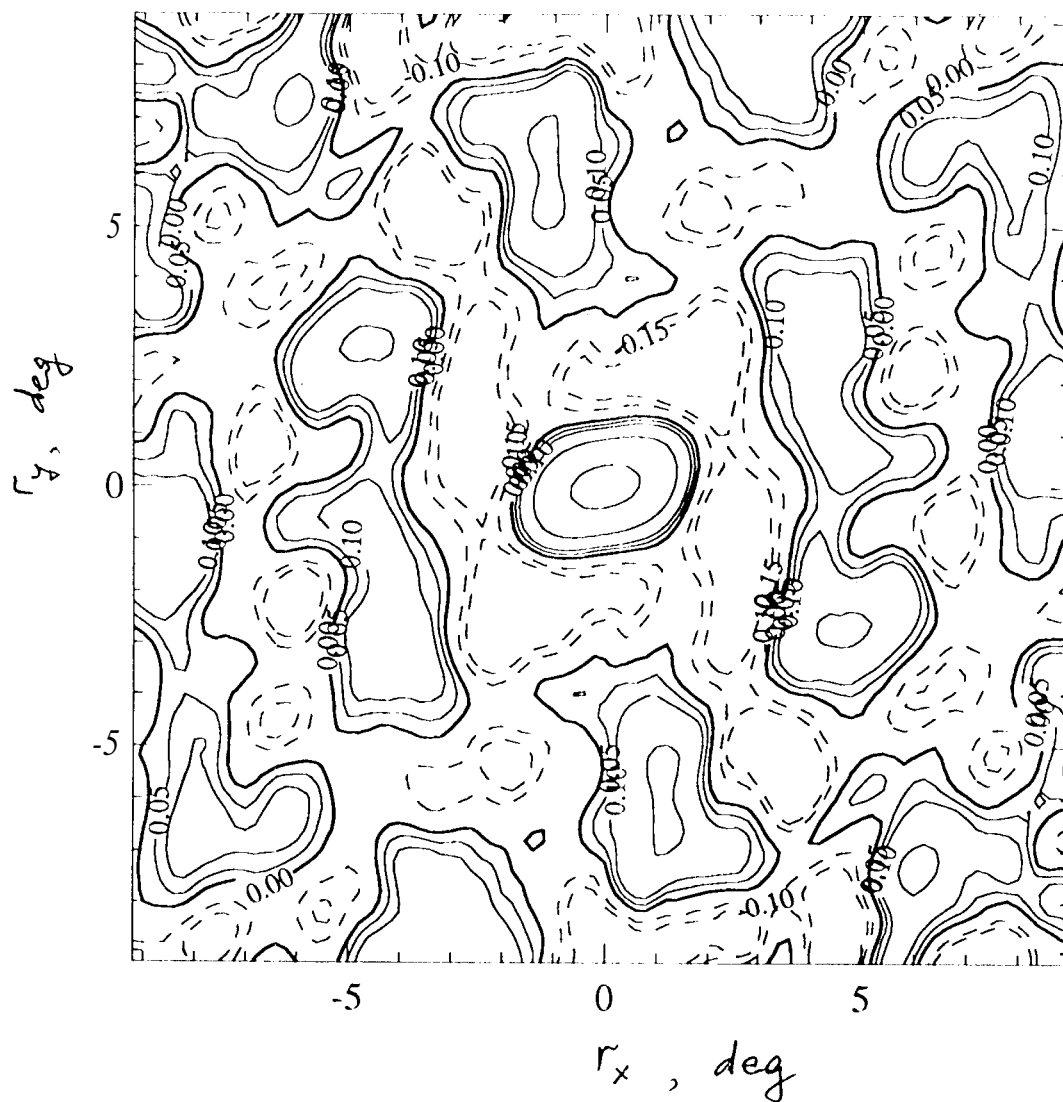


Fig 4.





Contours are drawn at intervals of 0.05

0.05, 0.10, 0.15, 0.20

F.g. 7

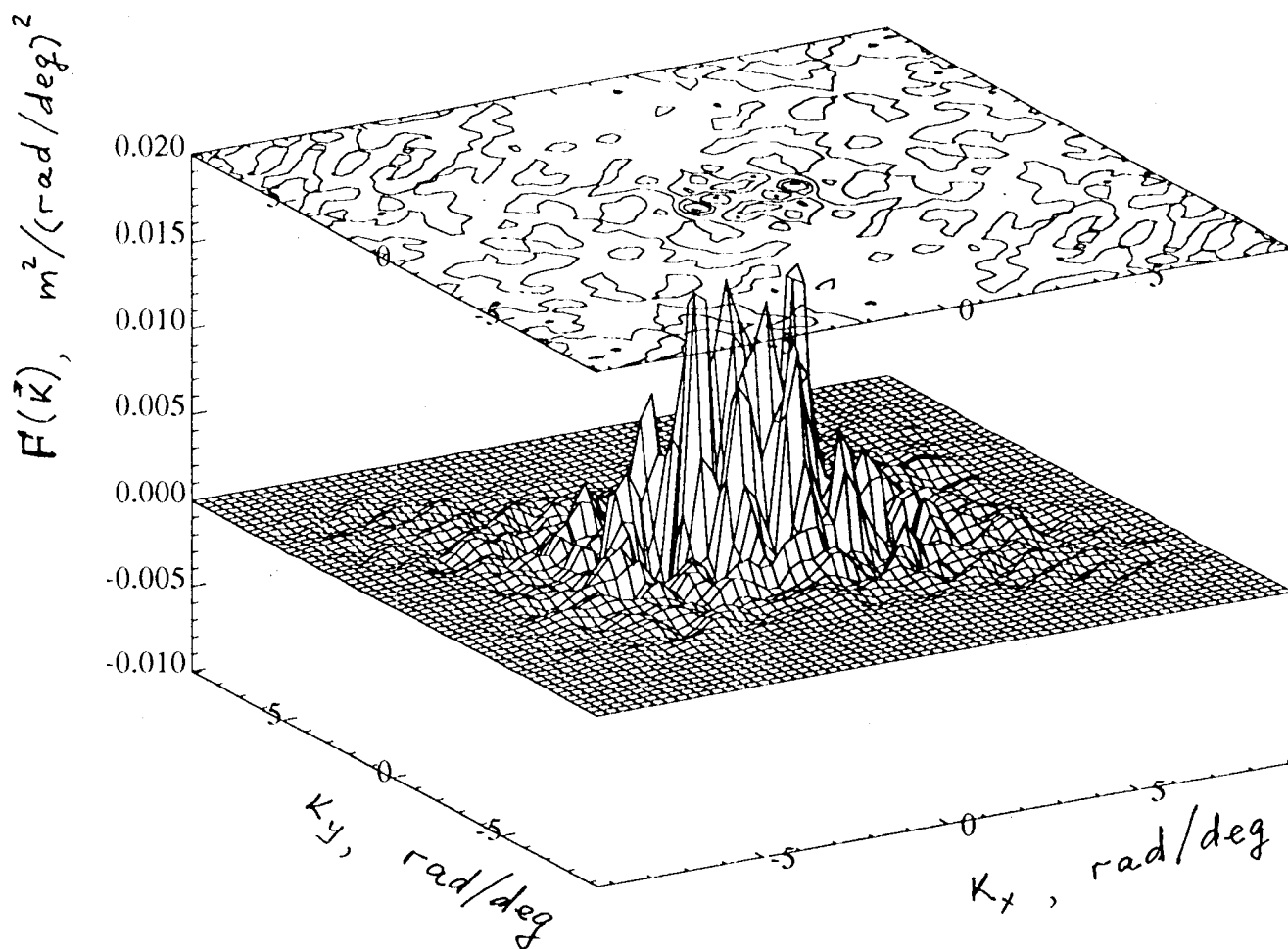
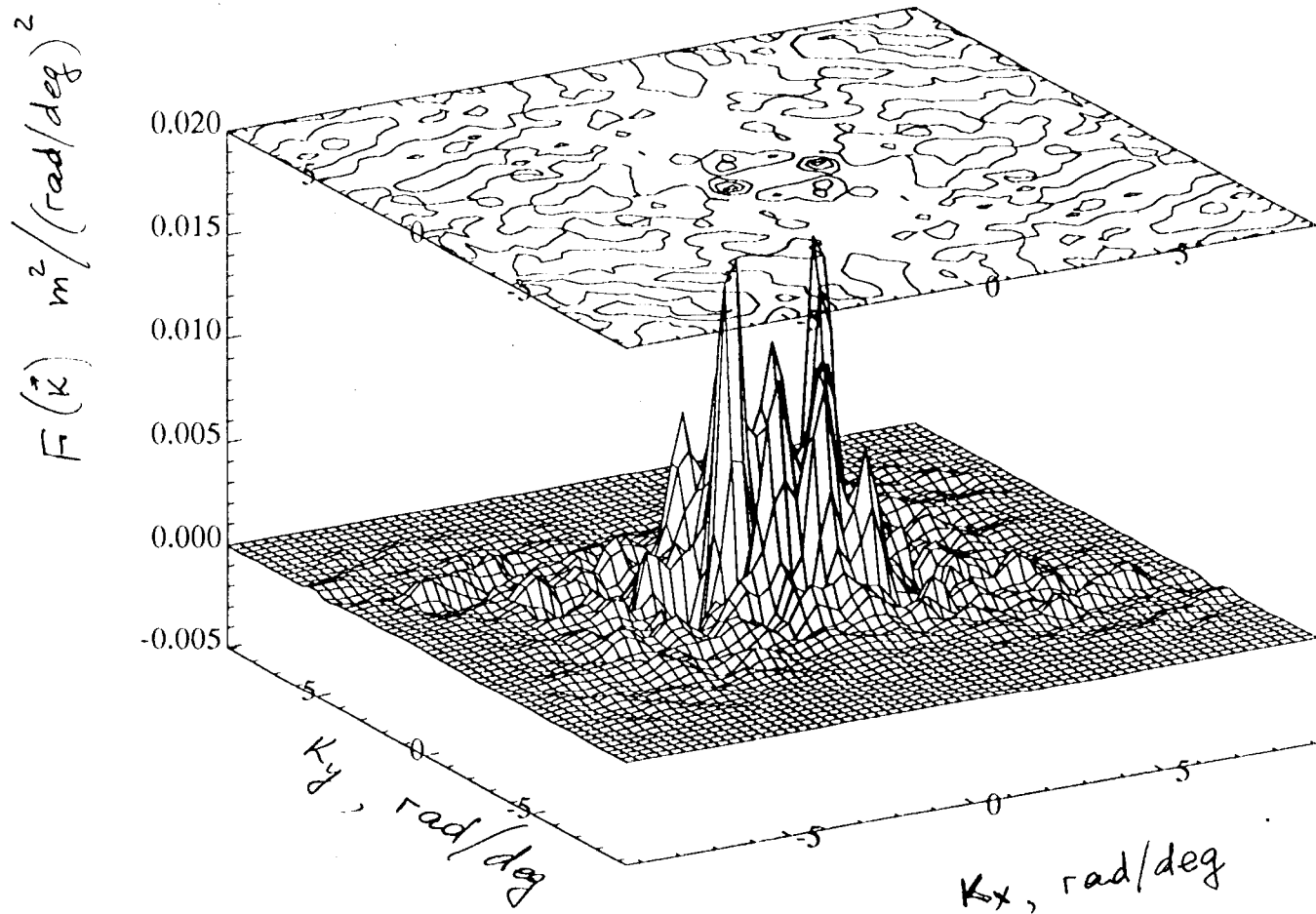


Fig. 5



$\vec{k}$   
 $\vec{k}$

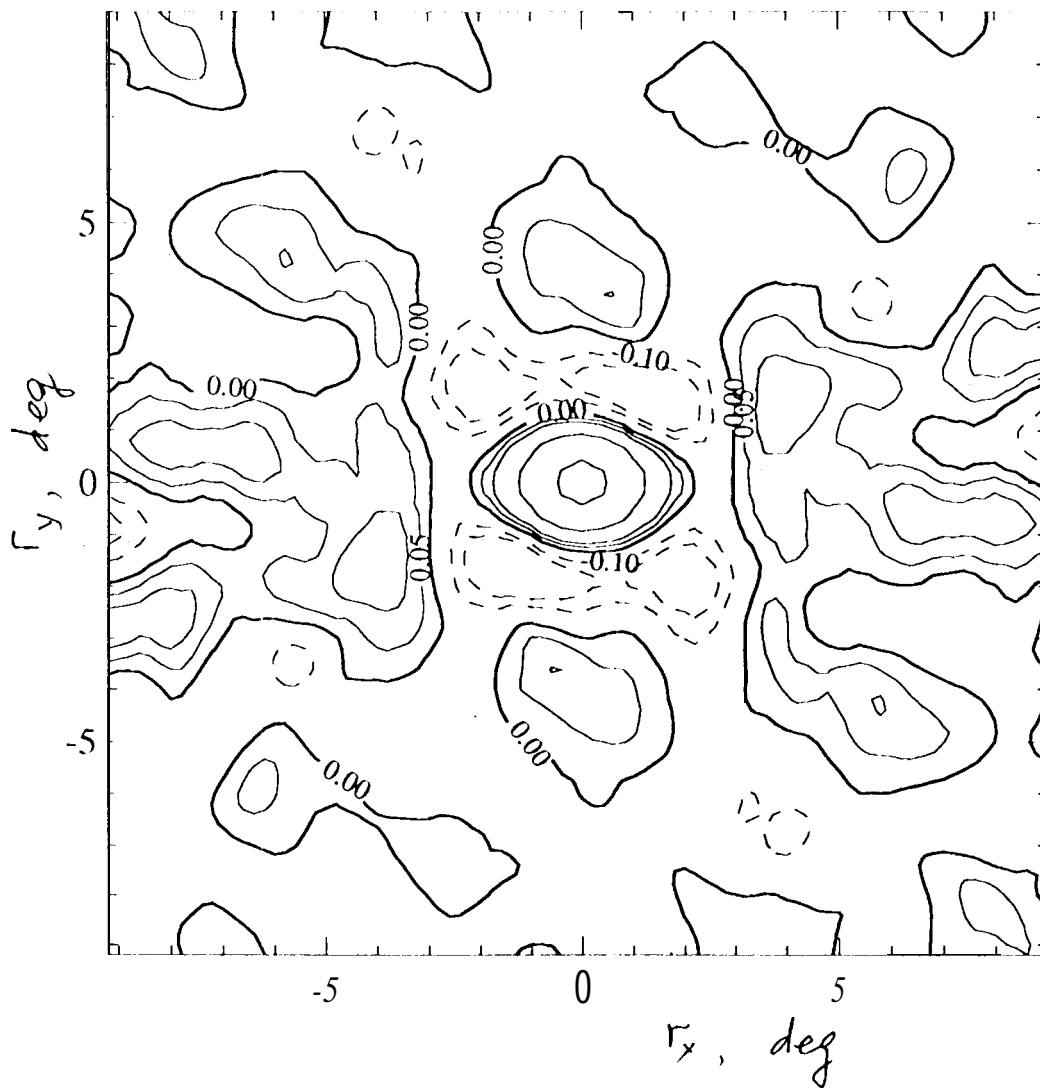
area

(1) (2) (3) (4) (5) (6) (7) (8) (9) (10) (11) (12) (13) (14) (15) (16) (17) (18) (19) (20) (21) (22) (23) (24) (25) (26) (27) (28) (29) (30) (31) (32) (33) (34) (35) (36) (37) (38) (39) (40) (41) (42) (43) (44) (45) (46) (47) (48) (49) (50) (51) (52) (53) (54) (55) (56) (57) (58) (59) (60) (61) (62) (63) (64) (65) (66) (67) (68) (69) (70) (71) (72) (73) (74) (75) (76) (77) (78) (79) (80) (81) (82) (83) (84) (85) (86) (87) (88) (89) (90) (91) (92) (93) (94) (95) (96) (97) (98) (99) (100)

"1"

37

Fig. 8



1.1

1.16 1.21, 1.25, 1.30

1.35 1.40, 1.45, 1.50

1.55 1.60, 1.65

1.70

-0.15

-0.10

0.00

0.05

0.10

0.15

0.20

Fig. 9

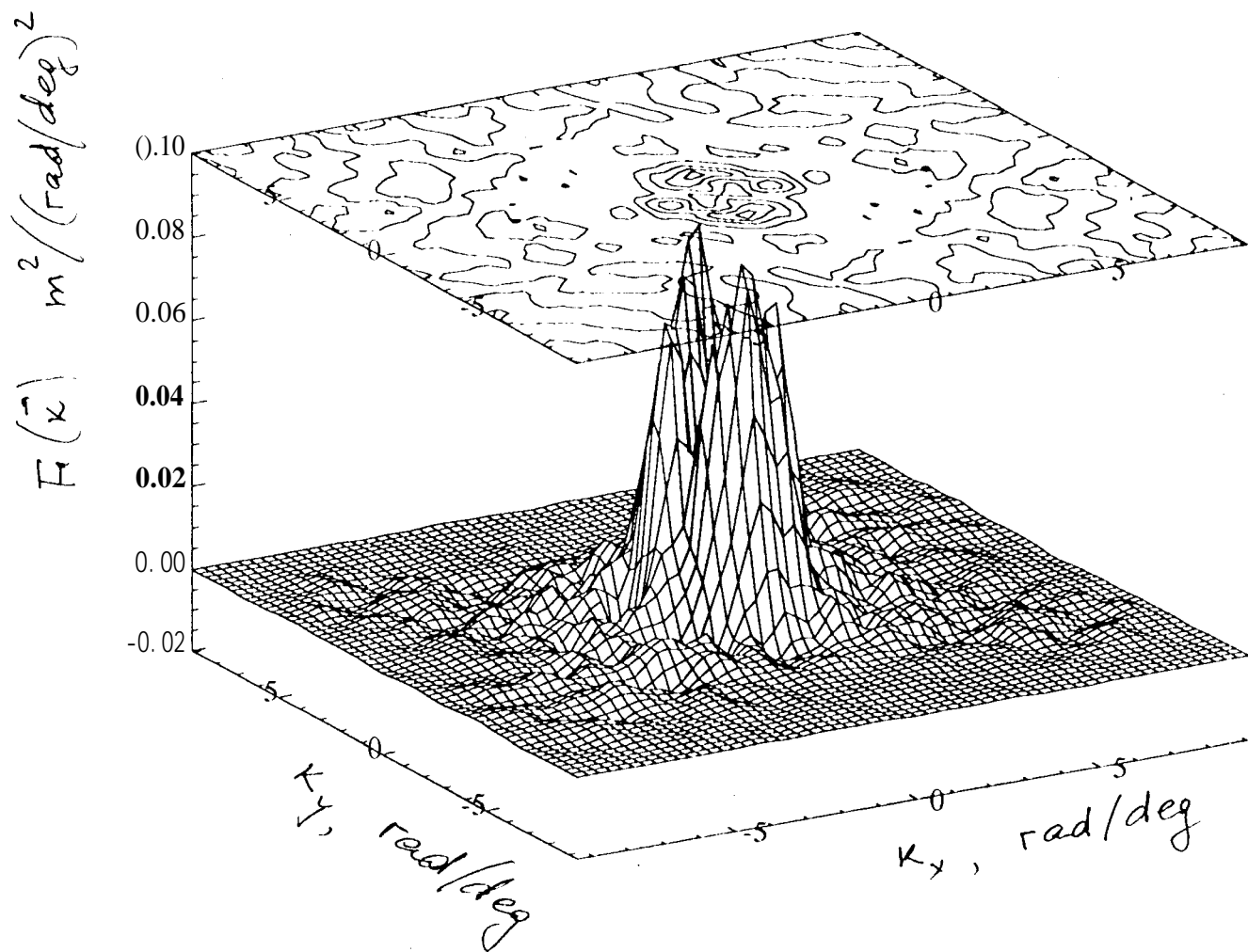


Fig. 10



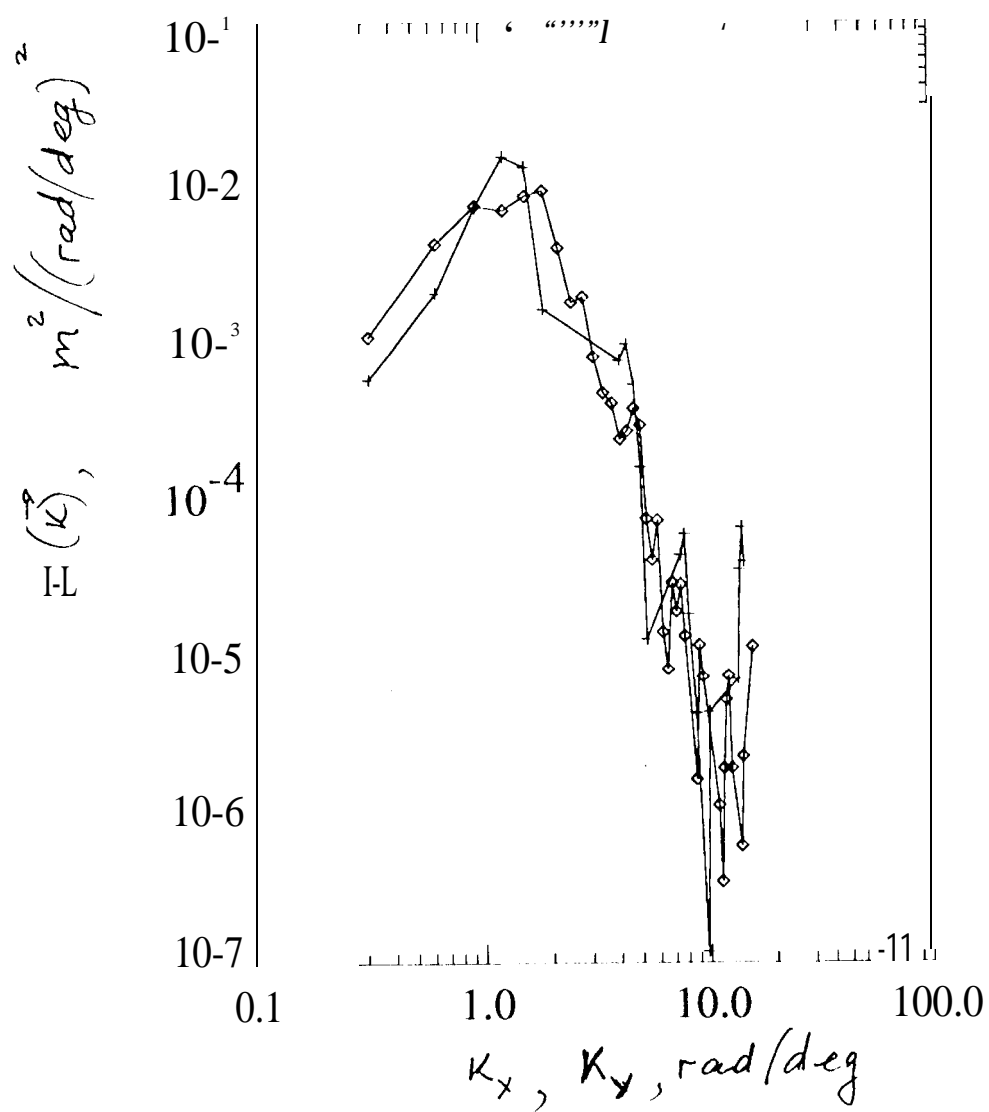


Fig. 11 A.

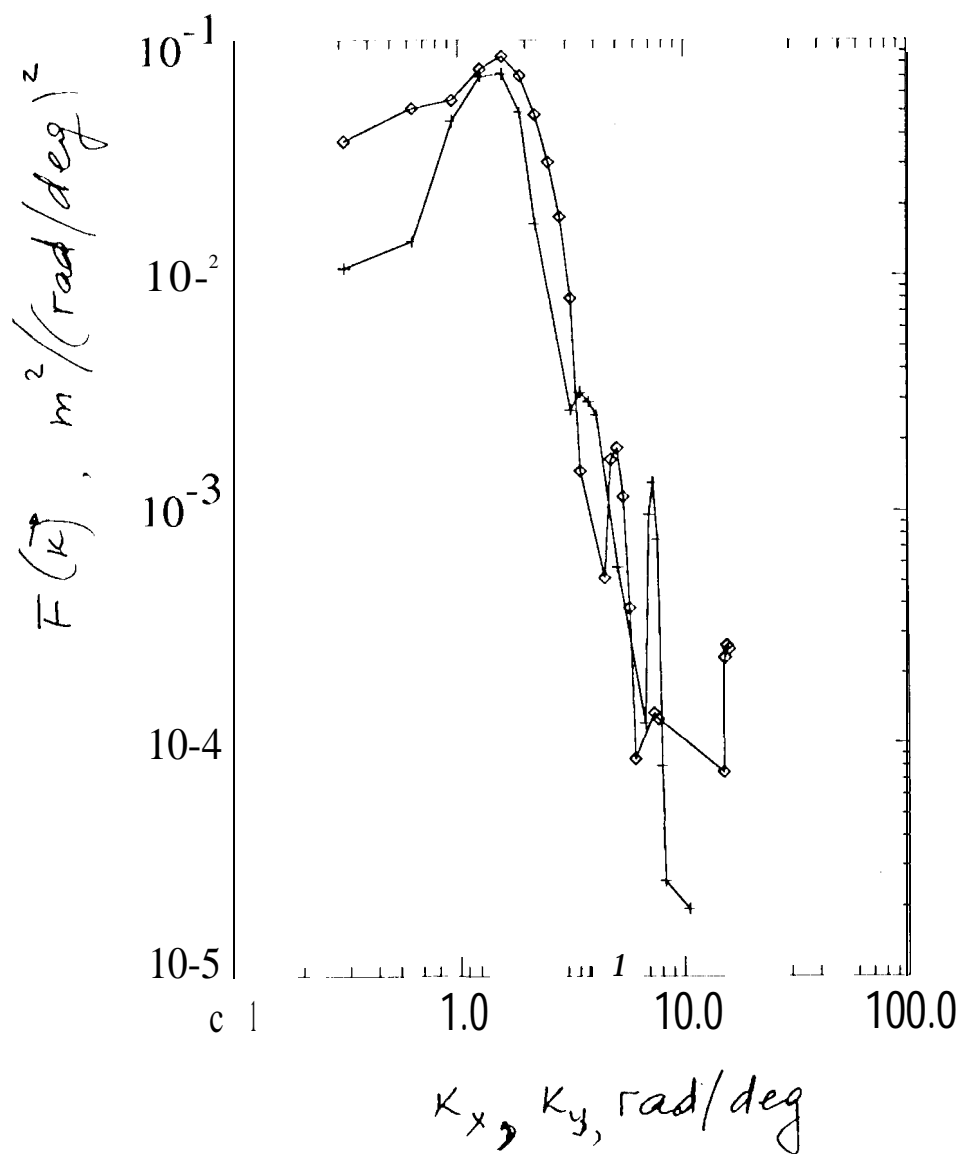
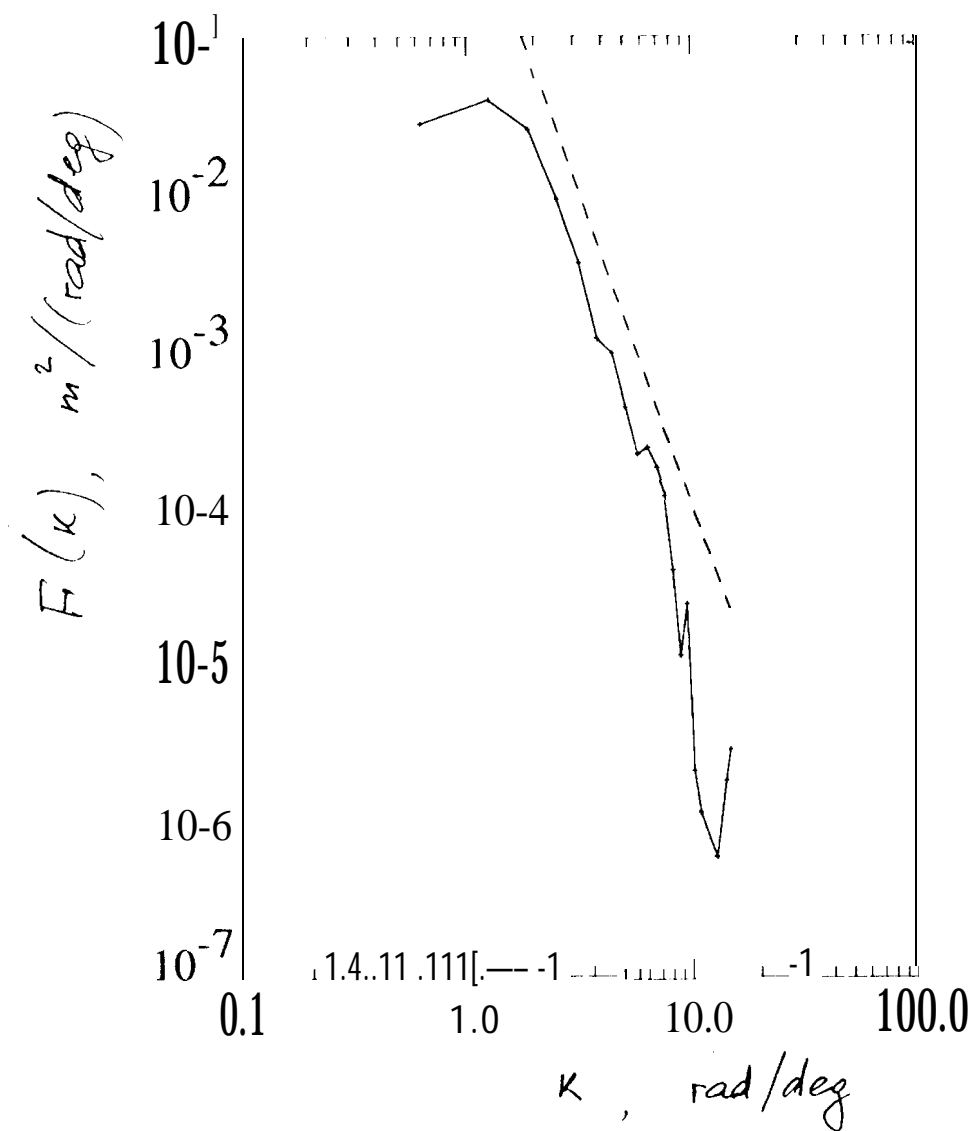


Fig. 12 B



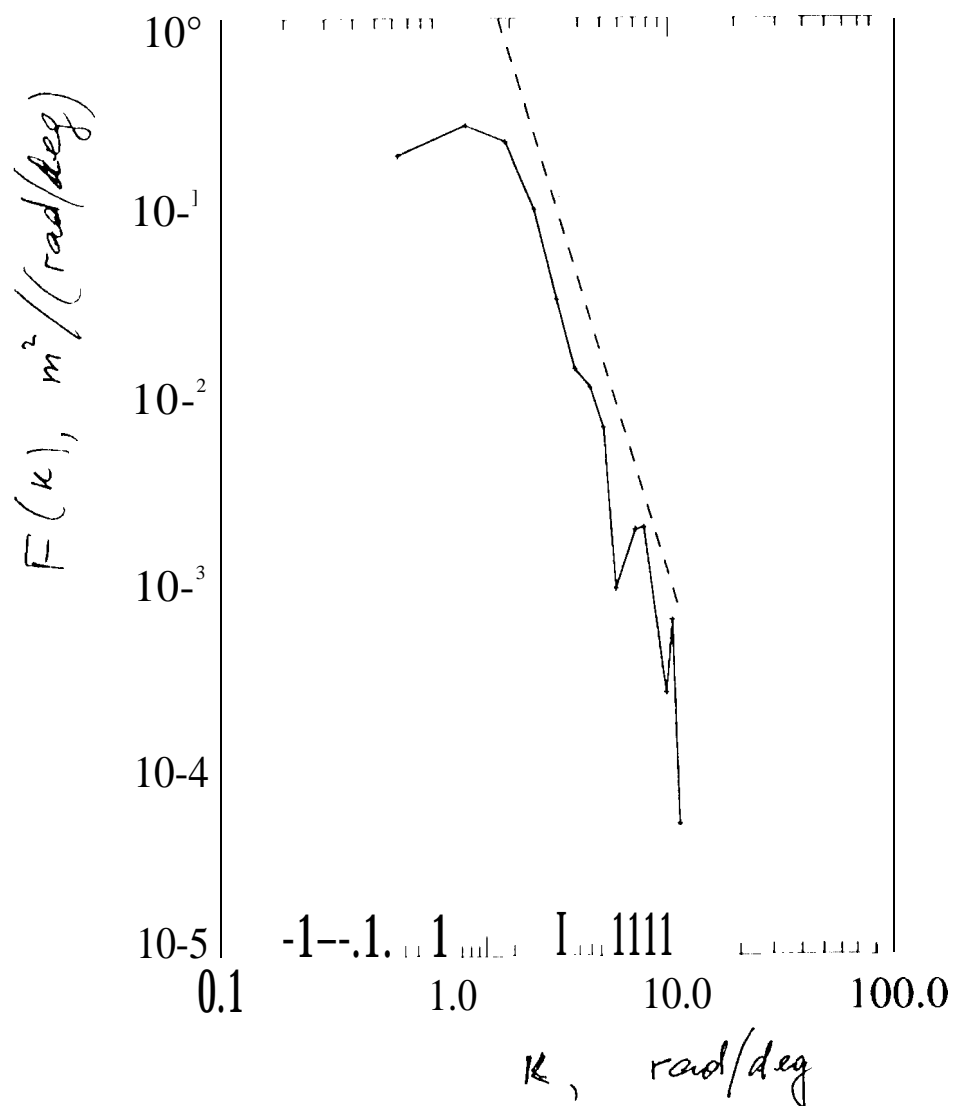


Fig. 12. B

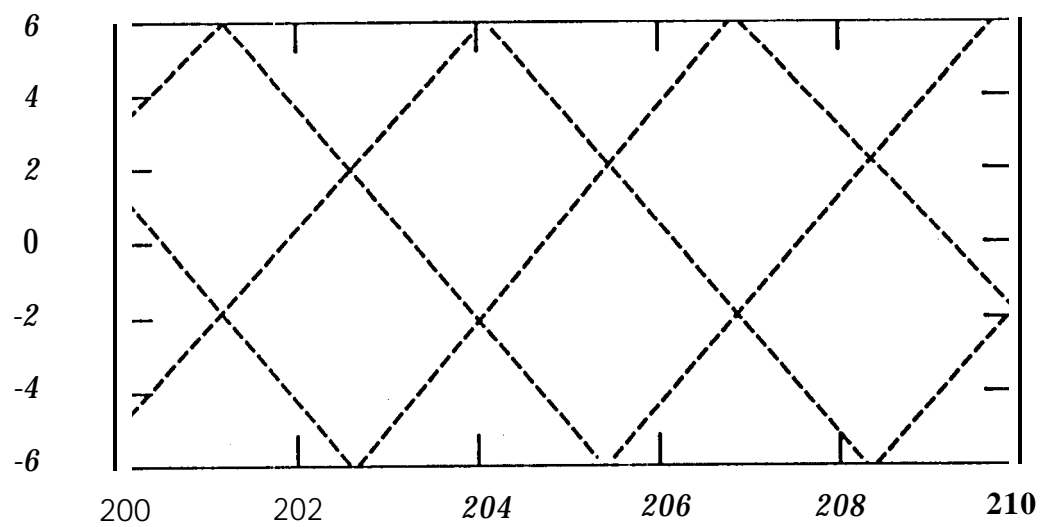
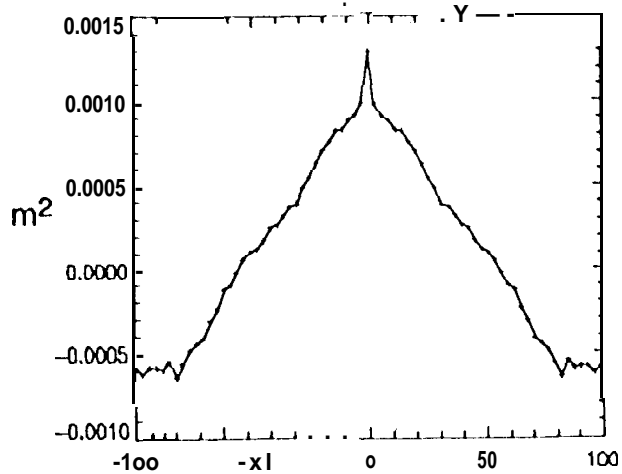
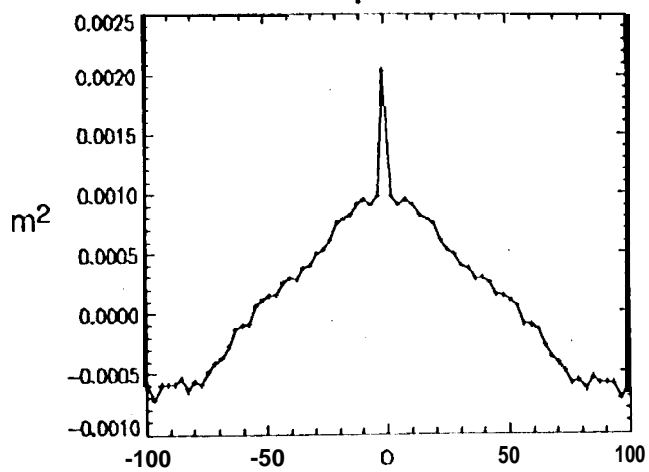
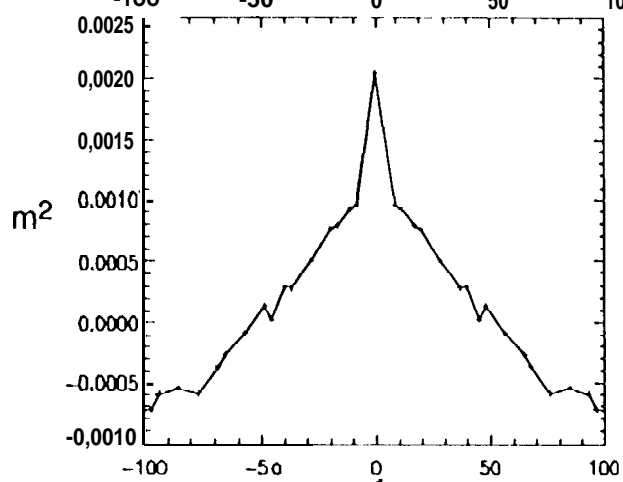
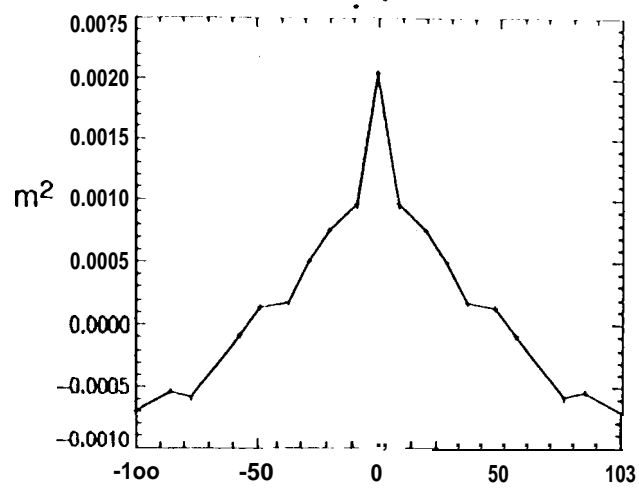
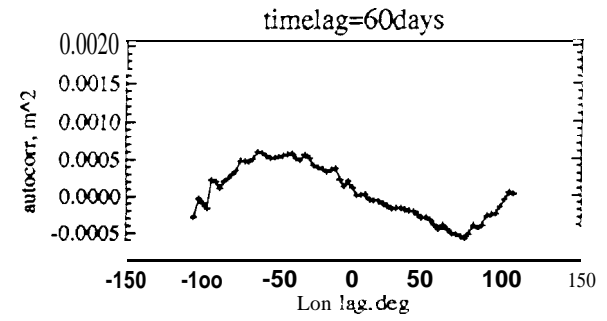
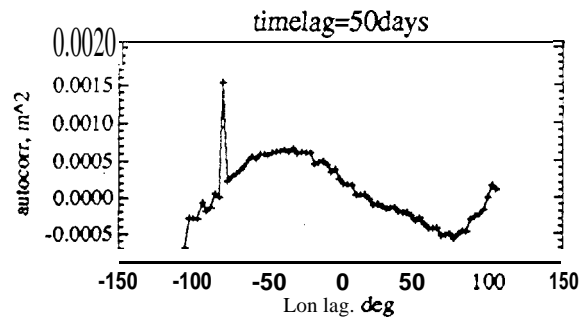
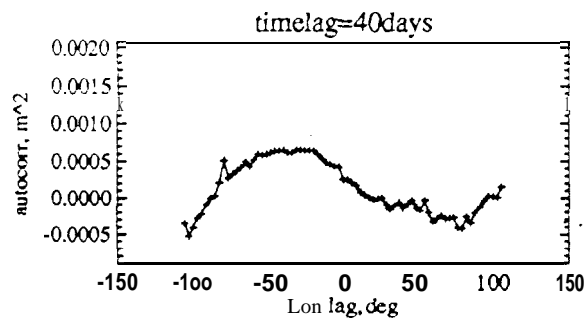
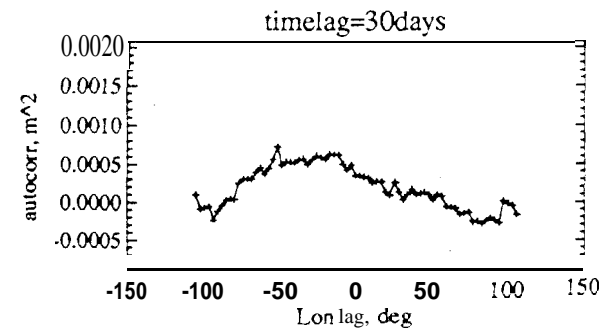
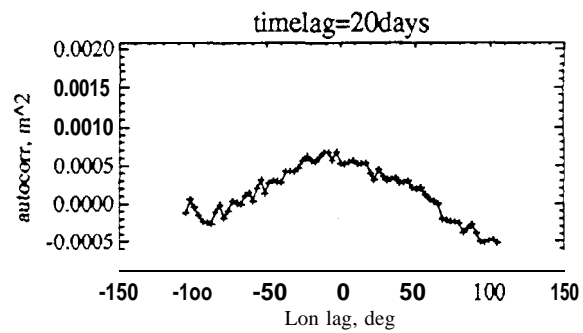
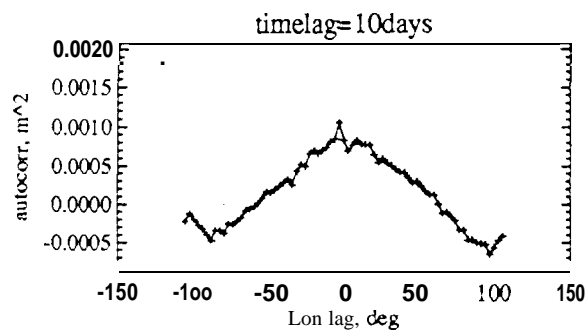
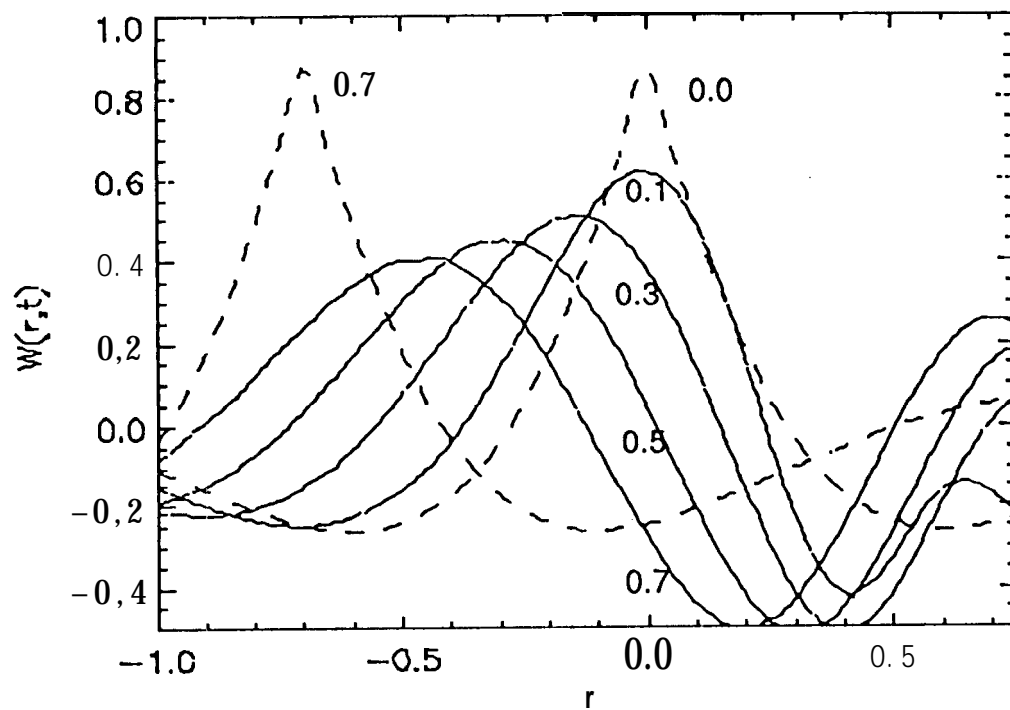


Fig.13 T/P altimeter ground tracks in an Equatorial Pacific region. Numbers are geographic coordinates.



Longitude lag, deg





( $Q = 3, \epsilon = 0.1$ )

Fig. 16